Experimental study of turbulent coherent structures using Particle Image Velocimetry and hydrogen bubble visualisation techniques

Xuan Zhang[1,2,3], Richard Simons[2], Jinhai Zheng[1,3]

1. College of Harbor, Coastal and Offshore Engineering, Hohai University, Nanjing, China
2. Department of Civil, Environmental and Geomatic Engineering, University College London, Gower Street, London, WC1E 6BT, UK
3. Key Laboratory of Coastal Disaster and Defence (Hohai University), Ministry of Education, Nanjing, China

Abstract:

The characteristics of coherent structures in turbulent boundary layers were investigated experimentally using PIV and hydrogen bubble visualisation techniques. Turbulent boundary layers were generated and tested in two flumes with different scale, for two Reynolds numbers: Re=32000 and 71200, both over a smooth bed. Measurements from the PIV technique and hydrogen bubble visualisation lead to the same research findings, suggesting a linear relationship between the instantaneous integral spatial scale and the instantaneous spacing between turbulent streaks. This new approach to determining the streak spacing provides some guidance for experimentalists in terms of experimental methodology. Results of hydrogen bubble visualisations provide additional evidence that streamwise vortices reside near low-speed streaks. Detailed statistical analysis further demonstrates the better performance of Burr distribution for the probability density function of streak spacing. Combining the measurements of flow field in the horizontal and vertical plane, streamwise vortices are observed to be tilted $\pm 8^{\circ}$ in the (x, z) plane and shear layers are inclined to the wall at 30° in the (x, y) plane.

Keywords: Fluid dynamics; turbulence; bottom boundary layer; coherent structures; Particle image velocimetry; hydrogen bubble visualisation.

Declarations

Funding

This work was supported by the UCL Dean's Prize and the China Scholarship Council (CSC), National Natural Science Foundation of China (Grant No. 51909074), China Postdoctoral Science Foundation (Grant No. 2019M661713), and Key Laboratory of Coastal Disaster and Defence of Ministry of Education, Hohai University (Grant No. 201912).

Conflicts of interest/Competing interests

There is no conflict of interest associated with this publication.

Availability of data and material

Thousands of PIV images and hydrogen bubble images made it infeasible to upload here.

Code availability

Yes.

Authors' contributions (optional: please review the submission guidelines from the journal whether statements are mandatory)

All authors contributed to the study conception and design. Material preparation, data collection and analysis were performed by Xuan Zhang. The first draft of the manuscript was written by Xuan Zhang and all authors commented on previous versions of the manuscript. All authors read and approved the final manuscript.

1. Introduction

Over the past few decades, noticeable progress has been made towards a more comprehensive understanding of turbulent boundary layers. Unidirectional turbulent currents have been shown to be influenced by hairpin vortices, which are often referred to as coherent structures. These vortices are believed to be the dominant feature in turbulent boundary layers (Robinson, 1991; Grass, 1971; Grass et al., 1991, 1993; Adrian et al., 2000; Dennis, 2015). Results from laboratory experiments and numerical models have made it clear that such coherent structures can be fundamentally classified into two types: the arch (alternatively known as hairpin or horseshoe) vortex and the 'quasi-streamwise' vortex (Bakewell and Lumley, 1967; Blackwelder and Eckelmann, 1979; Smith and Metzler, 1983; Kasagi et al., 1986; Stretch, 1990; Jeong et al., 1997; Lagraa et al., 2004; Jiménez, 2013). Horseshoe vortices are typical features with an asymmetrical or partially rolled-up form (both apparent in spanwise and streamwise vorticity); 'quasi-streamwise' vortices imply that they are meandering in the streamwise direction. Low-speed streaks, which are observed to be persistent and relatively quiescent most of the time in viscous sublayers, provide evidence for the counter-rotating streamwise vortices which form legs of hairpin vortices. These are linked to the phenomenon of 'bursting', a physical process described as a gradual uprising of the streaks, sudden oscillation, bursting and ejection (Corino and Brodkey, 1969; Kim et al., 1971).

Previous studies have examined the characteristics of coherent structures by experimental and numerical methods. Kline et al. (1967) was the first to observe the surprisingly well-organised spatially and temporally dependent motions within the viscous sublayer, leading to the formation of low-speed streaks very near the wall. Hydrogen bubble visualisation showed that the non-dimensional mean spanwise spacing between the low-speed streaks $\lambda^+ = \frac{\bar{\lambda} \cdot u_*}{\nu} = 100$ ($\bar{\lambda}$ is the mean spanwise spacing between low-speed streaks, u_* is the shear velocity, ν is the kinematic viscosity, and y is the distance from the wall). Smith and Metzler (1983) found that $\lambda^+ = 100$ is valid only at the edge of the viscous sublayer where $y^+ = \frac{y \cdot u_*}{\nu} = 5$ and further revealed that the value of λ^+ increases linearly with y^+. The probability density function of λ was observed to yield a log-normal distribution. Grass (1971) and Grass et al. (1993) demonstrated that wall-layer streaks are common features of turbulent flows over smooth and rough boundaries. The dominant spanwise spacing λ was found to be proportional to the bed roughness size, which reflects the typical scale of near-wall vortical structures. The streamwise extent of those streaks is generally in the magnitude of 600 to 1000 viscous lengths ($\frac{\nu}{u_*}$), as observed in laboratory experiments by Smith and Walker (1998). Numerical simulations (Robinson, 1991) further reveal that the low-speed streaks are commonly more than 1500 viscous lengths, with widths ranging from 20 to 80 viscous lengths. High-speed streaks are typically less than 600 viscous lengths, with widths varying between 40 and 110 viscous lengths. The method of quadrant analysis of Reynolds shear stress has been widely adopted in studies of turbulence to identify ejection events and investigate the contributions to Reynolds shear stress. Wallace et al. (1972) found that ejections and sweeps contributed 70% and 60% to the Reynolds shear stress in the region $20 \leq y^+ \leq 100$. At the point y^+=15, ejections and sweeps each contributed 70%. The dominance was observed for ejections away from the balance point (y^+=15) and for sweeps towards the wall. Lu and Willmarth (1973) showed that on average, 77% and 55% of the Reynolds shear stress originated from ejection and sweep events respectively. In contrast to Wallace et al. (1972), Lu and Willmarth (1973) found that the dominance of ejections over sweeps existed throughout the boundary layer. Brodkey et al. (1974) observed that ejections dominated over sweeps in the region $y^+ \geq 15$. They reported values of 80% and 60% in the region $30 \leq y^+ \leq 100$. The DNS results of Kim et al. (1987) suggested the crossing point y^+=12. Schultz and Flack (2007) suggested values of 85% and 75% in the region $y \leq 0.2\delta$ (δ was the boundary layer thickness). The relative strength of Q2 and Q4 to the Reynolds shear stress increased from 1.1 to 1.2 in the region $y \leq 0.4\delta$ and continuously increased up to the edge of the boundary layer. Mejia-Alvarez and Christensen (2010) reported values of 72% and 65% at $y = 0.1\delta$. Their results showed that ejections dominated over sweeps throughout the whole boundary layer. Min (2013) suggested equivalent values of 69% and 63% in the near-wall region ($y^+ \leq 80$). The conceptual model of a single horseshoe vortex initially put forward by Theodorsen (1952) has been investigated by many experimentalists (Grass et al., 1991, 1993; Haidari and Smith, 1994; Adrian et al., 2000; Lee et al., 2008). Results confirmed the existence of single horseshoe/hairpin vortices and demonstrated their close association with ejection and sweep events in the turbulent boundary layer, although no consensus on the characteristics has been reached.

Coherent structures have been found to play a crucial role in carrying turbulent energy and contributing to Reynolds shear stress (Grass, 1971; Robinson, 1991; Grass et al., 1991, 1993; Adrian and Liu, 2002; Jiménez, 2013). Low-speed streaks in viscous sublayers, when lifted up and resulting in bursts, have been noted to be responsible for turbulent energy production and make large contributions to Reynolds stress. All these cyclic physical processes lead to boundary layer turbulence being self-sustaining, converting kinetic energy from the mean flow to turbulent fluctuations and then dissipating by viscous processes.

Previous studies have shown that coherent motions such as bursting motions are closely associated with suspension of sediment (Sutherland, 1967; Heathershaw and Thorne, 1985; Nelson et al., 1995; Gyr and Schmid,

1997; Lelouvetel et al., 2009; Keylock et al., 2014). The essential properties of coherent motions, i.e. causing bed shear stress fluctuations, lead to successive saltations of particles. Parting lineation is a form of sand-bed configuration, referring to streamwise streaks consisting of low parallel ridges on the surface induced by a steady current (Sleath, 1984). Low-speed regions cause sand to accumulate while high-speed streaks lead to sand being washed away by the fluid. The spanwise spacing of parting lineation coincides with the mean spacing of turbulent streaks.

Although there have been many investigations of coherent structures in turbulent boundary layers, the geometrical and physical features of turbulent coherent structures are not well understood. There still lacks a comprehensive experimental study on the characteristics of coherent motions. The main objective of the present research is to carry out a detailed experimental study on the coherent structures over a smooth bed with the aims of providing additional knowledge and shedding light on the complicated physical processes in the bottom boundary layer.

This paper is organised as follows. Section 2 describes detailed information of the experimental set-up, followed by the data analysis methods given in section 3. Section 4 discusses the main results and findings from the small-scale and large-scale flume. Concluding remarks are stated in section 5.

2. Experimental Set-up

2.1 Laboratory flumes

The experiments were carried out in two parts: i). in the low-turbulence flume experiments; ii). In the 16m flume experiments. Figure 1 presents photographs of (a) the low-turbulence flume, (b) the laser, and (c) the camera for PIV measurements in the vertical plane (which will be described in section 2.2), taken from the side. The current was supplied by a pumped recirculation system [see Figures 1 (d) and (e)], with the inlet fed from a constant-head tank and the outflow going via a calibrated collection tank into an underground sump. A submersible pump returned the water from the sump to the constant-head tank. The constant head tank had an adjustable weir inside, which was linked to a float and maintained a constant water level by increasing or decreasing the level of the weir when any changes occurred. An orifice plate was located in the base of the constant head tank to provide coarse control of the flow rate. Measurements of the flow rate were obtained by recording the time for a specific rise of the water level in the calibrated collection tank at the outlet. This procedure was repeated three times and the mean value adopted, leading to an accuracy of 1cm/s in the flow rate. The main flow then went through the orifice plate and into the inlet tank.

The UCL 16m flume was used for the second set of experiments. The pumping system included a monitoring system to check water levels in the supply tank. This allowed generation of a steady turbulent current.

For more details of the two flumes and the flow conditions, the reader is referred to Zhang and Simons (2019).

(a)

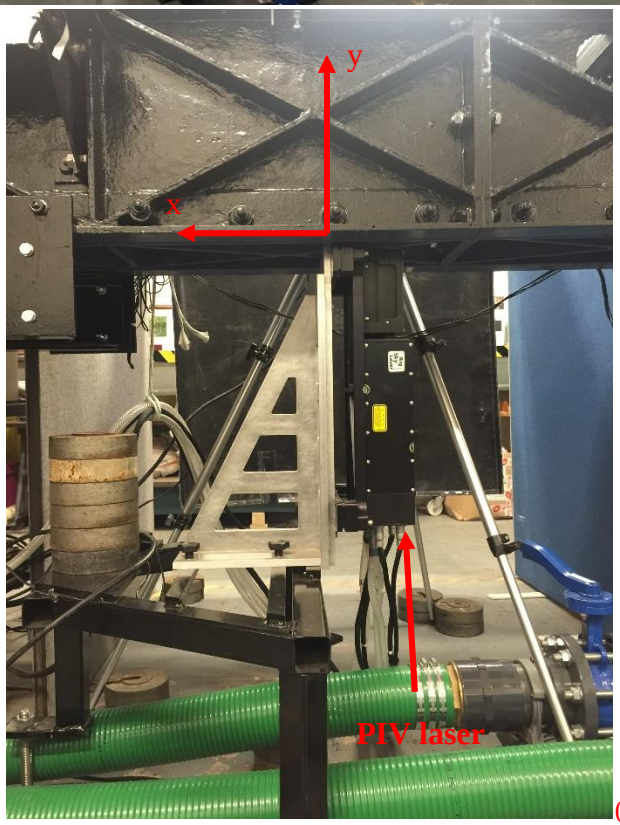

(b)


y
z
x
Camera

(c)

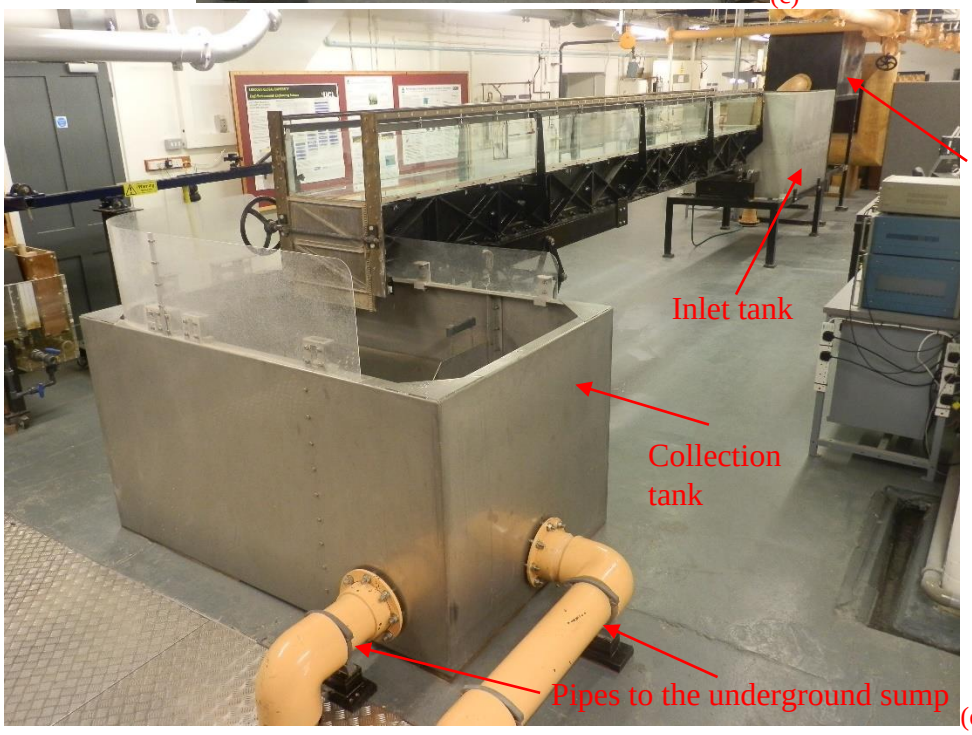
Constant-head tank
Inlet tank
Collection tank
Pipes to the underground sump

(d)

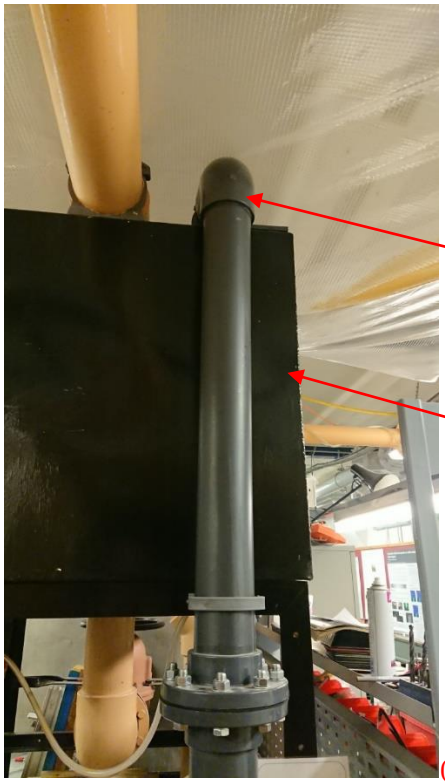

(e)

Figure 1. Low-Turbulence flume experiments: (a) side view of the flume; (b) PIV laser; (c) camera position; (d) hydraulic installation of the whole flume; (e) Inlet pipe from the submersible pump.

2.2 Particle Image Velocimetry (PIV)

A PIV system was used to obtain velocity measurements in both the horizontal and vertical planes. A double pulsed Nd:YAG 120-15 BSL Laser (532nm wavelength) was used to produce the laser light sheet. This was characterized by high-energy pulses (150mJ per pulse) with short pulse durations (8ns), leading to a short exposure time for each photographic frame. A 12 bit CCD camera (630059 POWERVIEW Plus 4MP PIV camera) was used to capture a sequence of images illuminated by the laser. The seeding particles used in the present study were composed of fused borosilicate glass (ASTM C169) and were hollow non-porous microspheres. The density of the particles was 1.10 ± 0.05 ($g \cdot cm^{-3}$), which was close to the water density. The flow was seeded with hollow microsphere particles (10% < 5µm, 50% < 10µm, 90% < 21µm and 97% < 25µm) by a seeding device placed at the inlet. A seeding tank was used together with a perforated tube, connected together using a hose. Seeding particles were added into the header tank, which was filled with water. The seeding particles then flowed through the hose into the perforated tube, which distributed them uniformly across the inlet tank. The current and particle mixture passing through the ballotini glass beads, the mesh and the contraction at the inlet ensured homogeneous distribution in the flume. The whole seeding system was found to perform well, distributing the seeding particles while not disturbing the flow. A synchronizer box (610035 LaserPulse Synchroniser) was adopted to trigger the PIV externally. This connected the computer, frame grabbers, camera, laser, and the data board that ultimately synchronised all these devices through the corresponding channel.

2.3 Hydrogen Bubble Visualisation

In the present study, the hydrogen bubble visualisation technique was used to facilitate understanding of the streaky patterns in the near-wall region and to validate the results obtained from the PIV system. This is a technique commonly adopted to examine vortex structures (e.g. Chung et al., 2016). The electrical current was supplied by a pulse generation box 'CEV47601' and applied to a fine platinum wire. The supporting system used for the present investigations consisted of a traverse with a micrometer adjustment, a carriage, a support arm with a pulley, and two brass supports. A traverse with a micrometer adjustment was attached to the support arm through the carriage, which could be moved up and down so as to control the fine movement of the wire accurately.

2.4 Experimental procedures

For the PIV experiments in the low-turbulence flume, velocity measurements in the horizontal plane were made by capturing 600 pairs of images sequentially. Each pair of images covered an area 76mm (streamwise direction) × 76mm (spanwise direction). The key parameter when optimising PIV results is the time dt between frame A and frame B, which was adjusted to obtain the best quality of data. According to the manual, there are five rules dominating the quality of velocity determinations: i) Interrogation window size should be small enough for one vector to precisely represent the flow kinematics; ii) There need to be more than 10 particle pairs within each interrogation spot; iii) The maximum in-plane displacements for each image pair should be 1/4 of the interrogation spot size; iv) The maximum out-of-plane displacements should be 1/4 of the laser light sheet thickness; v) The minimum in-plane displacements should be twice the particle diameters (in pixels). In the present experiments, dt=800μs was adopted so that the rules given above are satisfied. This led to a small number of interpolated vectors (less than 5% of the whole sample). The images were analysed to determine velocity vectors by the Insight 4G software. A recursive Nyquist grid was adopted to process the acquired images in two iterations: an interrogation area of 64 pixels×64 pixels in the first iteration and 32 pixels×32 pixels in the final one. The first iteration determined velocity vectors using a 50% overlapping rule. Results of the first iteration were then used for optimising the spot grid during the second iteration. The local displacements were determined by a FFT cross-correlation algorithm (Insight 4G Manual; Adrian, 1991). A Gaussian peak was adopted for locating the correlation peak, based on fitting a 3-point Gaussian in x direction and 3-point Gaussian in z direction with the peak pixel used in both. This routine leads to higher spatial resolution as compared with the Nyquist grid and faster speed as compared with the deformed grid. The spatial resolution was 0.6mm/grid, which was fine enough to reveal detailed information in the bottom boundary layers. Post-processing was carried out by a universal median test within a neighbouring area of 3 pixels×3 pixels. The determination of PIV correlation peak displacement was accurate to within 0.1 pixel (Westergaard et al., 2003). This indicates that velocities were resolvable to within 4mm/s for the measurements in the horizontal plane obtained from the two flumes.

The whole procedure was repeated to obtain streamwise and vertical velocities, which gave Reynolds shear stress and velocity vectors demonstrating the spanwise vortices. The PIV measurements were obtained by illuminating the vertical plane with the laser. For each of the conditions tested in the present study, each pair of images covered an area of 195mm (streamwise direction) ×195mm (vertical direction). The time dt=2600μs was adopted to optimise the data quality, based on different camera set-ups. Processing led to a spatial resolution of 1.4mm/grid, slightly coarser than that mentioned above. This indicates that velocities were resolvable to within 3mm/s for the measurements in the vertical plane obtained from the two flumes.

In order to set up the hydrogen bubble experiments, a pair of thin copper plates was stuck to each sidewall inside the flume at the same level above the bed. The plates were 3.5cm wide and 8cm high for one, and 4.5cm wide and 17.5cm high for the other. They were positioned at the test section (2.5m from the inlet), with the lower edge of the larger one touching the flume bed and the smaller one 9.5cm from the bed. This was observed to give more uniform generation of bubbles along the wire, compared with using just one pair on one sidewall. Stuart (1984) found that the wire diameter generally acts as a good approximation to the bubble diameter. Thus, the diameter of hydrogen bubbles was taken to be 0.025mm in the present study. The wire was cleaned both chemically and mechanically before starting video recording. The method of reversing the polarity of the electrical circuit and applying the electricity current for approximately 20s was observed to be effective in removing the deposited salts on the wire and increasing the quality of hydrogen bubble visualisations. Having completed the cleaning work, the electrical current was applied to the wire and left running for 20s. This step was found to be necessary to ensure the quality of hydrogen bubble visualisation since the quantity of bubbles increased at the initial stage until it reached a steady state. Having checked that the bubbles generated were good, and the flow had recovered from the disturbance caused by the cleaning work, the hydrogen bubble pulse generator was switched on and the camera started.

The spatial resolution for the 16m flume was not much different from the small-scale experiments, with the horizontal plane covering an area of 73mm (streamwise direction) × 73mm (spanwise direction) and the vertical plane of 195mm (streamwise direction) ×195mm (vertical direction). These led to a spatial resolution of 0.6mm/grid and 1.5mm/grid, respectively. Post-processing was carried out by a universal median test within a neighbouring area of 9 pixels×9 pixels, which was larger than that adopted in the low-turbulence flume because of the larger scale involved.

3. Data Analysis methods

Most of the methods for data analysis follow section 3 of Zhang and Simons (2019). In this paper, additional information is given for determining the statistical characteristics of the spacing between low-speed streaks in turbulent boundary layers. Having obtained the time series of streak spacing, statistical analysis is then performed to investigate the standard deviation σ_λ, coefficient of variation ψ_λ, skewness S_λ, and flatness F_λ using the following definitions:

$$\sigma_\lambda = \sqrt{\frac{1}{N-1}\sum_{n=1}^{N}[\lambda(t)-\bar{\lambda}]^2} \quad (1)$$

$$\psi_\lambda = \frac{\sigma_\lambda}{\bar{\lambda}} \quad (2)$$

$$S_\lambda = \frac{\frac{1}{N-1}\sum_{i=1}^{N}[\lambda(t)-\bar{\lambda}]^3}{{\sigma_\lambda}^3} \quad (3)$$

$$F_\lambda = \frac{\frac{1}{N-1}\sum_{i=1}^{N}[\lambda(t)-\bar{\lambda}]^4}{{\sigma_\lambda}^4} \quad (4)$$

where N is the sampling number of the whole time series, $\lambda(t)$ is the instantaneous value of spacing between low-speed streaks, $\bar{\lambda}$ for the time-averaged mean streak spacing.

This is used for investigating the probability density functions of streak spacing. In the present study, a lognormal distribution and a Burr distribution were used. The probability density function of the lognormal distribution is represented as:

$$P(\lambda(t)) = \frac{1}{\lambda(t)\phi\sqrt{2\pi}}\, exp\left\{\frac{-[ln\lambda(t)-\mu]^2}{2\phi^2}\right\} \quad (5)$$

$$\mu = log\left(\frac{\bar{\lambda}^2}{\sqrt{\bar{\lambda}^2+{\sigma_\lambda}^2}}\right) \quad (6)$$

$$\phi = \sqrt{log\left(\frac{{\sigma_\lambda}^2}{\bar{\lambda}^2+1}\right)} \quad (7)$$

The Burr distribution is more flexible and can represent a wide range of distribution shapes. This was originally proposed by Burr (1942) as a distribution controlled by two parameters, and later developed by Tadikamalla (1980) with an additional parameter. The probability density function is given by:

$$P(\lambda(t)) = \frac{\frac{\xi\Omega}{\Upsilon}\left[\frac{\lambda(t)}{\Upsilon}\right]^{\Omega-1}}{\left\{1+\left[\frac{\lambda(t)}{\Upsilon}\right]^{\Omega}\right\}^{\xi+1}} \quad (8)$$

where ξ and Ω are the shape parameters and Υ is the scale parameter.

4. Results and Discussions

Results of mean velocity profiles and Reynolds shear stress distributions have been presented and discussed by Zhang and Simons (2019) and are not included here.

4.1 Low-speed streaks and high-speed streaks

Figure 2 gives a snapshot of hydrogen bubble visualisations. Streamwise vortices are detected by intertwined timelines of hydrogen bubbles, as indicated by orange arrows in the figure. These are observed to be where low-speed streaks locate, supporting the previous observation that counter-rotating streamwise vortices reside near turbulent streaks (Blackwelder, 1983; Smith and Schwartz, 1983; Kasagi et al., 1986; Jimenez and Kawahara, 2013). Low-speed streaks are formed where a pair of vortices bring flow up into the outer region, and high-speed streaks are where another pair of vortices rotating in the opposite direction bring flow down into the near-wall region. Experiments performed in a low Reynolds number water tunnel (Clark and Markland, 1971) identified these counter-rotating vortices in the wall region ($7 \leq y^+ \leq 70$). Results of the present study suggest that the streamwise vortices may also exist below the wall region.

Figure 3 shows contours of streamwise velocities for the 16m flume, with the time relative to the initial measurement given for each snapshot. Axes are based on the PIV coordinate system and denoted as 'Relative z' and 'Relative x'. The origin of each image is 200mm from the left sidewall, when viewed in the flow direction. Regions of high-speed and low-speed streaks are highlighted by red and black ellipses, and denoted as 'HSS' and 'LSS' respectively. Low-speed streaks are observed to be elongated in the streamwise direction and tend to meander in the spanwise direction. Applying the Taylor 'frozen turbulence' hypothesis (Taylor, 1938), these high-speed and low-speed streaks all move downstream approximately at the local mean velocity. In the spanwise direction, these streaky patterns are observed to locate randomly at any position and to be tilted to the x-direction. The maximum tilting degree is found to be 8°, with equally probable occurrence in both positive and negative sign.

A typical example illustrating streak merging is given in Figure 4. As can be seen from Figure 4 (a), five streaks exist at the image centre ('LSS1', 'LSS2', 'LSS3', 'LSS4', and 'LSS5'). The crowded streak distribution provides an opportunity for the merging process to occur. In the next image [Figure 4 (b)], the two neighbouring streaks ('LSS2' and 'LSS3') intersect and start to merge into one. This results in the merging of low-momentum regions. In Figure 4 (c), these two streaks have completed the merging process and become a wider low-speed streak. This merging process takes time of $\Delta t^+ = \Delta t \cdot \frac{{u_*}^2}{\nu} = 16$, leading to a wider spacing between low-speed streaks. Because of this merging process occurring repetitively, streak spacing varies in scale. The probability of each spacing is further discussed later.

In the streamwise direction, the low-speed streaks are observed to occupy the entire measurement window from Figure 4(a) to Figure 4(c). Therefore, the streamwise length of low-speed streaks must be longer than 210mm

(1550 viscous lengths). By combining all the contour plots sequentially into one long picture (see Figure 5 for a typical example of part of the picture), the flow field can be investigated in an Eulerian frame of reference. Detailed observation of low-speed and high-speed streaks suggests that the streamwise length scale can extend up to 5180 and 2330 viscous lengths for low-speed and high-speed streaks, respectively.

As can be seen from Figure 5, high-speed streaks are relatively wider than low-speed streaks, agreeing with the typical characteristics of streaky patterns found by Robinson (1991). The characteristic width of low-speed and high-speed streaks reflects the spanwise scale of streamwise vortices and are observed to vary temporally and spatially. Detailed observation of all the contour plots suggests that the width of low-speed streaks (high-speed streaks) ranges between 7 and 110 (30 and 210) viscous lengths. Results show wider ranges than the numerical finding of Robinson (1991), where width of low-speed and high-speed streaks were observed to be 20-80 and 40-110 viscous lengths respectively.

Auto-correlations of streamwise velocity fluctuations are presented in Figure 6. A peak value of R is found to be located at the point dz=12mm [Figure 6 (a)], and the second peak located at twice this value, as expected for periodic signals. The value of 12mm, the instantaneous streak spacing λ, is consistent with the value from visual inspection of streaks [see Figure 6 (b) for the black line].

A linear relationship is observed between the streak spacing and the integral spatial scale. Results are illustrated in Figure 7 (a) and (b) for PIV measurements and hydrogen bubble visualisations in the low-turbulence flume. Those from the 16m flume are shown in Figure 8. Best-fit lines are shown in red. R-squared values suggest satisfactory results of curve fits. The linear relationship indicates that the spacing between low-speed streaks is 6 times the eddy size.

Based on the results above, it is concluded that λ is linearly related to the integral spatial scale I.S.S. This appears to be a common feature regardless of laboratory scale, water depth, and measurement techniques. The method is different from existing ones to determine the instantaneous streak spacing, which can be categorised into two types: i) visual counting (Kline et al., 1967; Smith and Metzler, 1983); ii) Fast Fourier Transform of the instantaneous spanwise distribution of streamwise velocities (Mansour-Tehrani, 1992; Grass et al., 1993). Results presented above suggest that the present method is more suitable when a large number of samples is available, and can be applied for further analysis of the mean streak spacing $\bar{\lambda}$ and probability density functions of λ.

Results of non-dimensional mean streak spacing yield 118 and 125 for the tests conducted in the low-turbulence flume and the 16m flume. All these values are close to although slightly higher than the values in the literature.

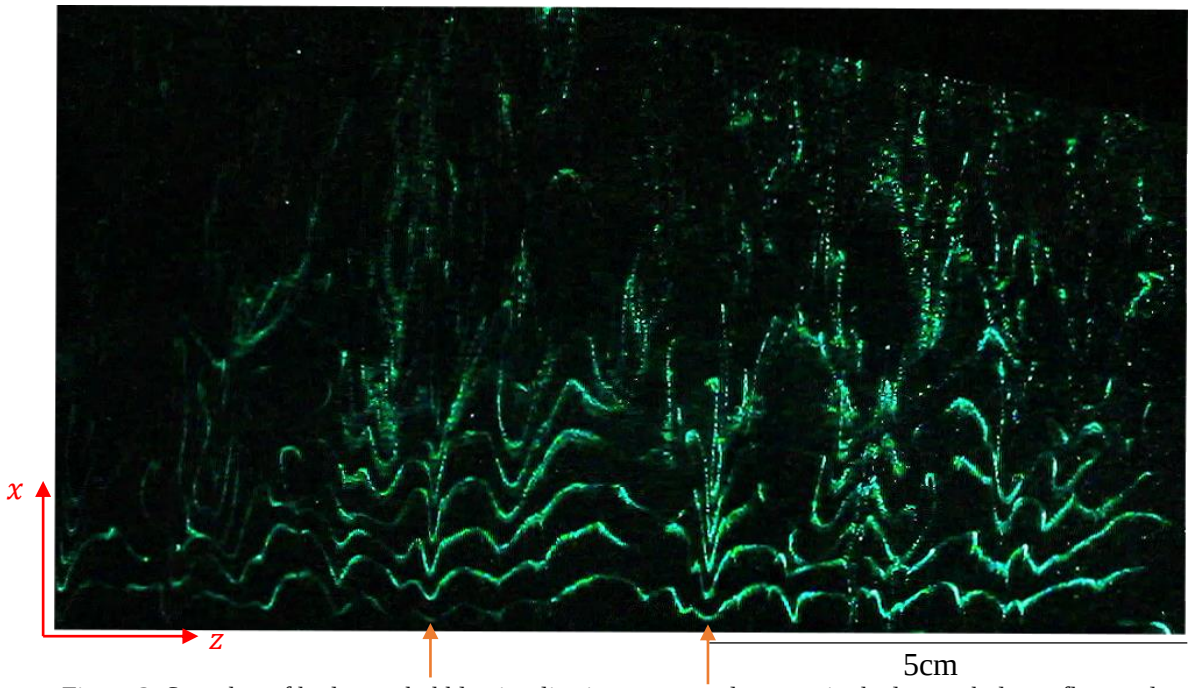

Figure 2. Snapshot of hydrogen bubble visualisation: current-alone test in the low-turbulence flume, plan view, y=0.8mm (y^+=6) above the bed, the current flowing from bottom to top.

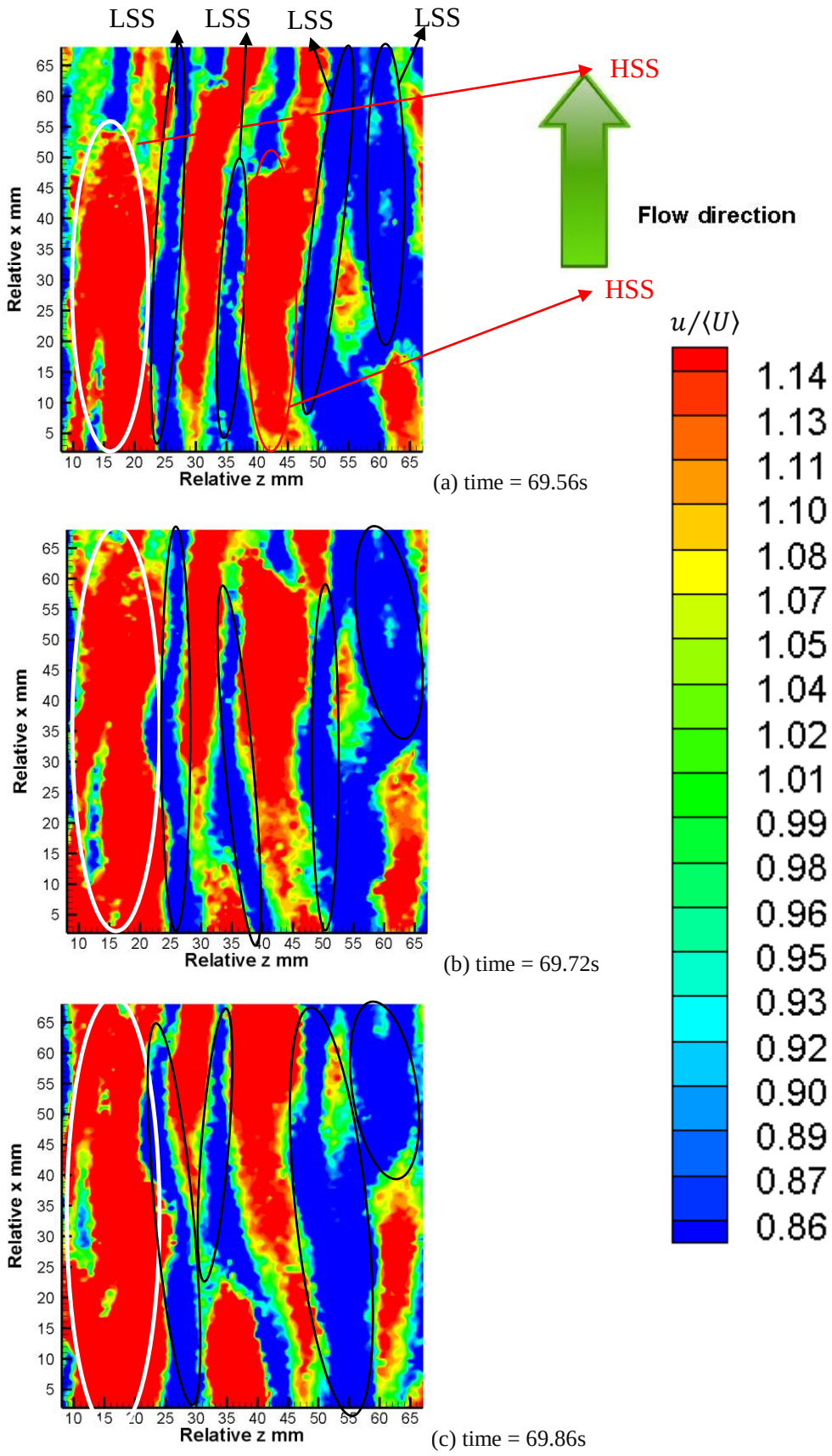

Figure 3. Time histories of instantaneous streamwise velocity contours from PIV measurements, 16m flume, plan view, y=0.8mm (y^+=6) above the bed. Note that values are normalised by the local mean velocity $\langle U \rangle$.

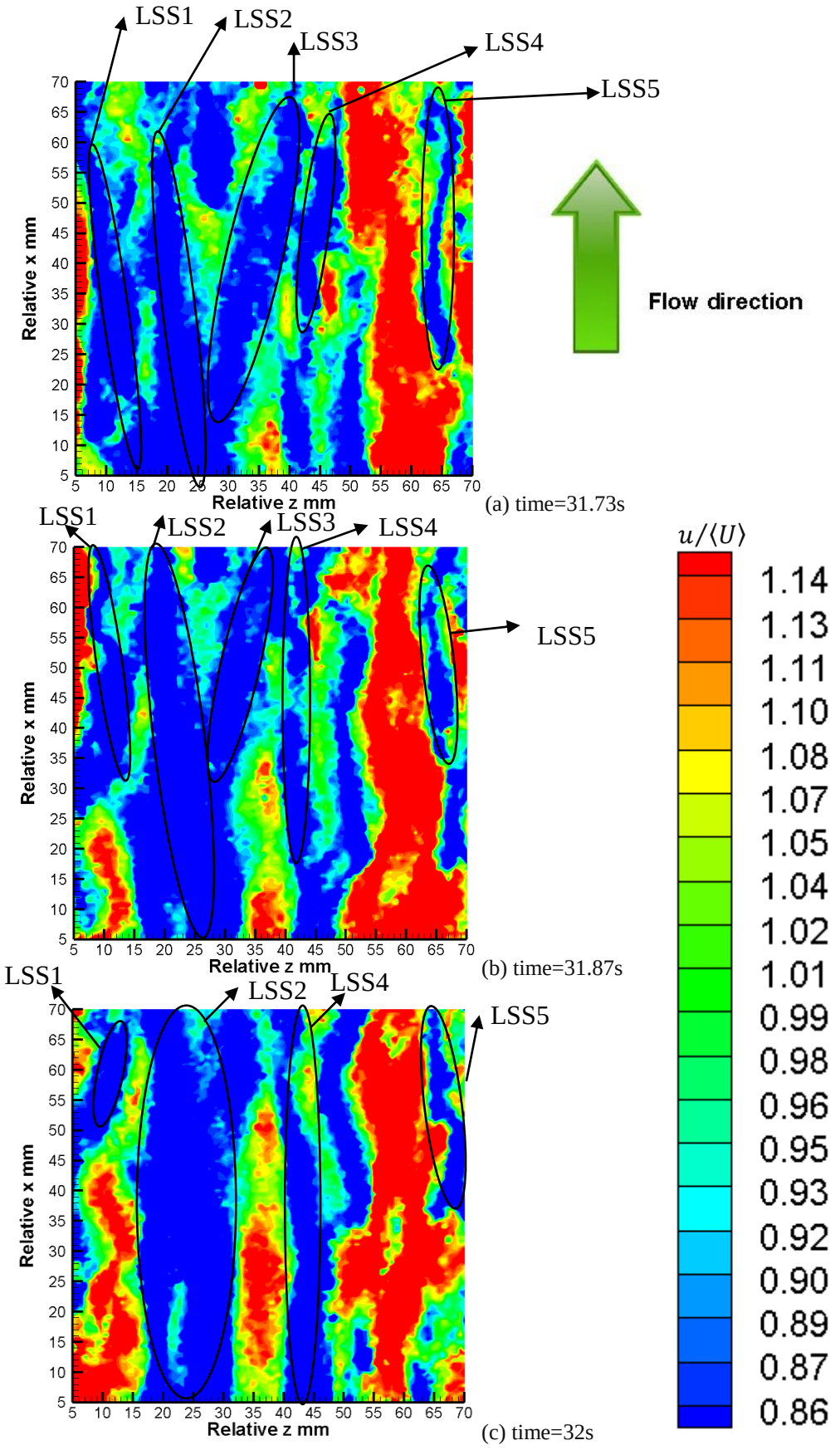

Figure 4. Time histories of instantaneous streamwise velocity contours, low-turbulence flume, plan view, y=0.8mm (y^+=6) above the bed. Note that values are normalised by the local mean velocity $\langle U \rangle$.

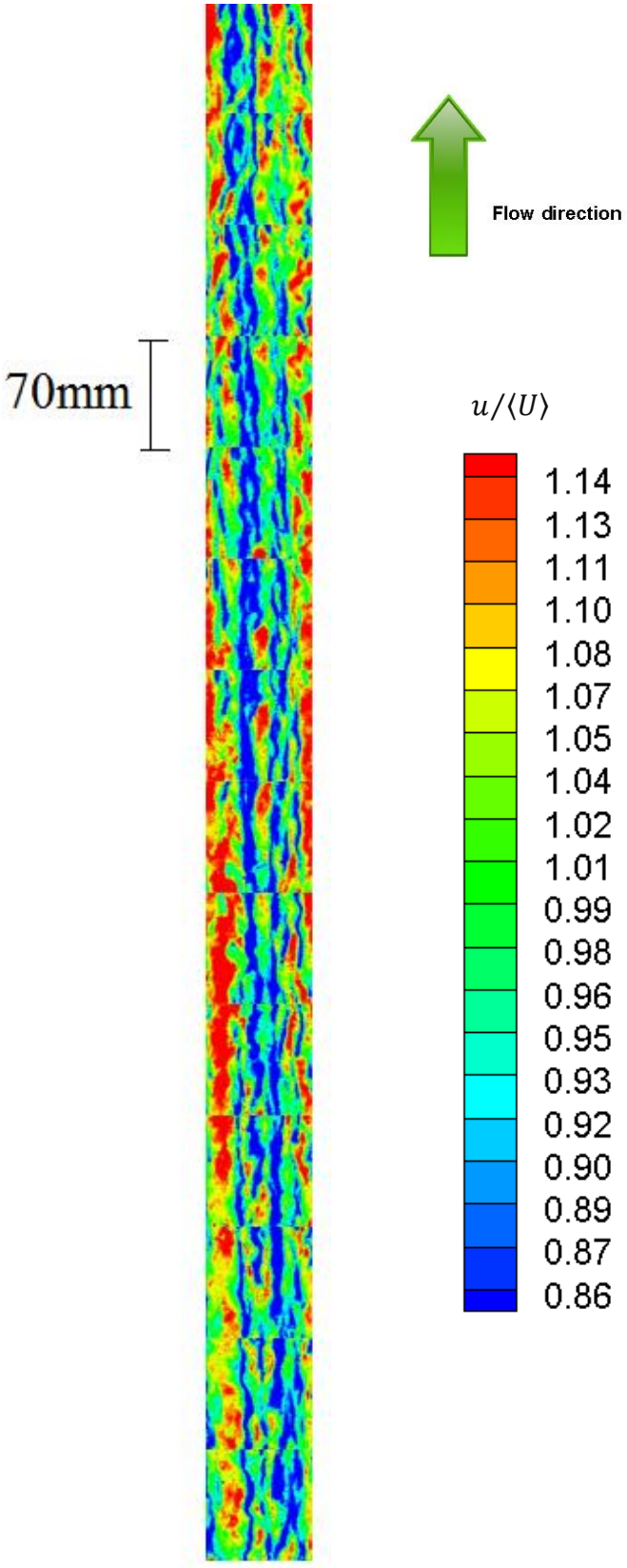

Figure 5. A typical example showing part of the long picture of instantaneous streamwise velocity contours, low-turbulence flume, plan view, y=0.8mm (y^+=6) above the bed. Note that values are normalised by the local mean velocity $\langle U \rangle$.

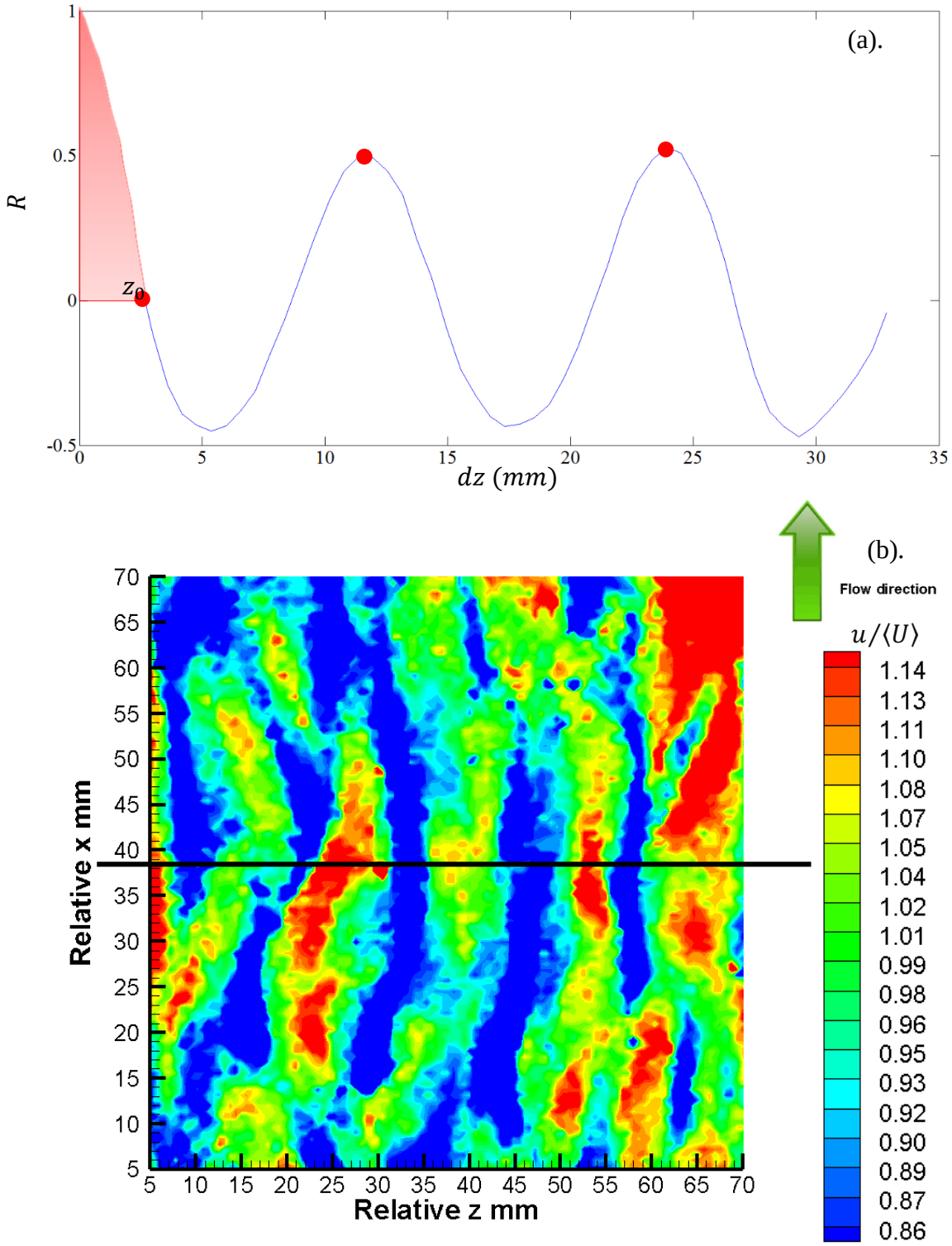

Figure 6. Instantaneous flow field at y = 0.8mm ($y^+ = 6$), PIV measurements of the unidirectional turbulent current, tested in the low-turbulence flume: (a) auto-correlation distribution of streamwise velocity at the image centre; (b) contour plots of streamwise velocity, values normalised by the local mean velocity given in the legend. Red dot shows the first zero-crossing point, red shadowed areas highlight the integral spatial scale before the first zero-crossing point ($I.S.S$).

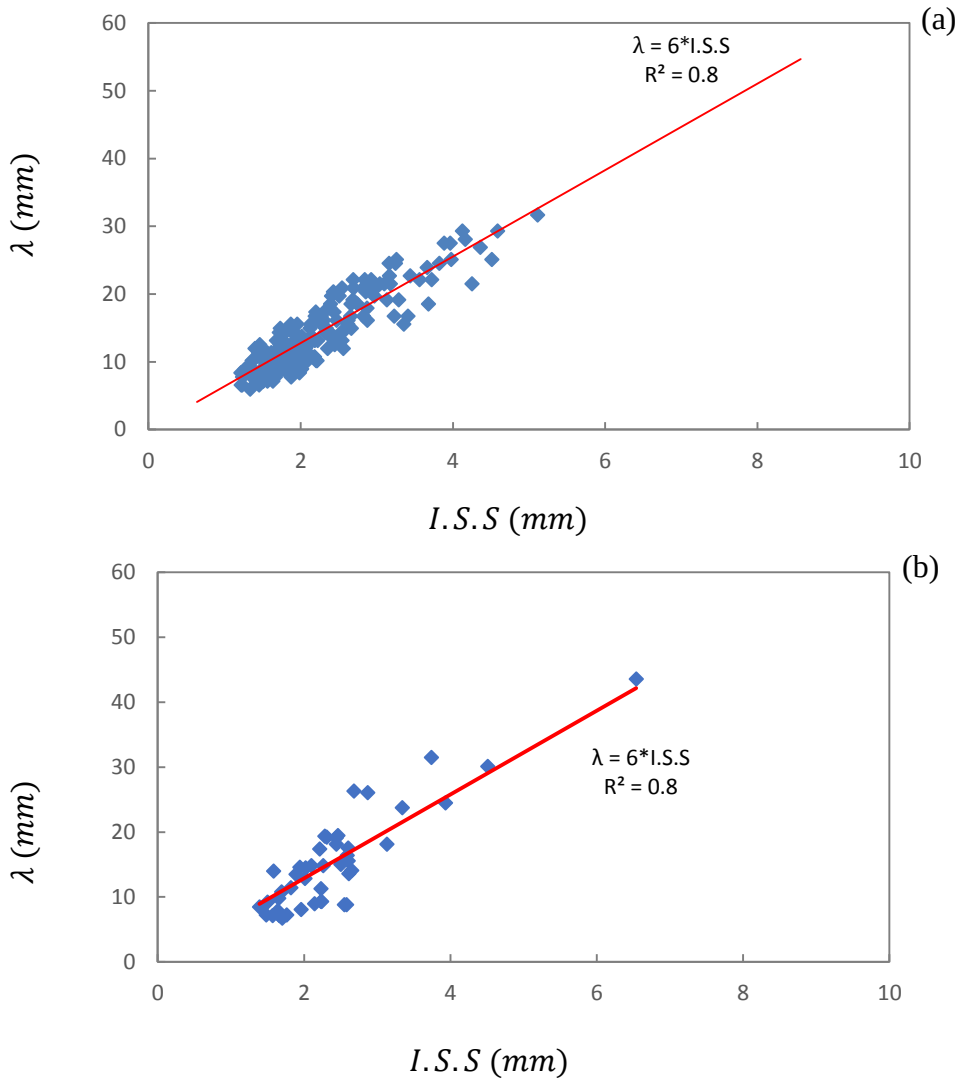

Figure 7. Streak spacing λ (mm) vs Integral Spatial Scale (mm). Turbulent current test in the low-turbulence flume: (a) PIV measurements; (b) hydrogen bubble visualisations.

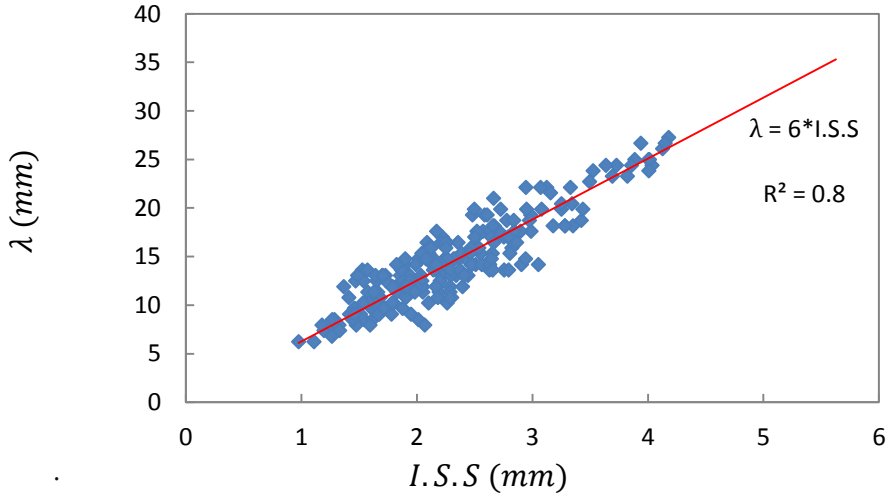

Figure 8. Streak spacing λ (mm) vs Integral Spatial Scale (mm). Turbulent current test in the 16m flume, PIV measurements.

Figure 9 illustrates the probability density functions of streak spacing for tests conducted in the low-turbulence flume, a) from PIV measurements; and, independently, b) from hydrogen bubble visualisation. Results show that the most probable value of the streak spacing λ_{most} is approximately 20% less than the mean value of streak spacing $\bar{\lambda}$ obtained from the two measurement techniques independently. A Burr distribution is found to fit the data better than a lognormal distribution. This is different from previous observations (Nakagawa and Nezu, 1981; Smith and Metzler, 1983; and Mansour-Tehrani, 1992). The better performance of a Burr distribution is reflected in the statistical parameters (Table 1). Although the coefficient of variation ψ_λ demonstrates a consistency between the two flumes and good agreements with previous experiments, values of the skewness and flatness are larger than those quoted in the literature. This indicates that the probability density functions are more peaked than a lognormal distribution as suggested by previous experiments. The higher probability of the peak value could be explained by the streamwise length scale of low-speed streaks. As demonstrated above, the flow field shown in an Eulerian frame suggests longer streamwise streak lengths than the values suggested by previous numerical studies. Therefore, those streaks should persist for a longer time and have higher probabilities to occur for the peak value.

The probability density function of streak spacing can be interpreted in terms of streamwise vortices meandering downstream. As discussed above, streamwise vortices locate near low-speed streaks. The close association between low-speed streaks and streamwise vortices indicates that the variability of streak spacing may be caused by 'footprints' of streamwise vortices. Therefore, either the occurrence of merging/splitting of streamwise vortices and/or the scale of streamwise vortices could be represented by a Burr distribution.

The probability density function of streak spacing has some implications for probabilistic models of turbulent events. Previous experiments of Nakagawa and Nezu (1981) suggest that the streak spacing and the time between bursts have the same probabilistic model. Hence the Burr distribution, which has been shown capable of predicting the streak spacing, may be generalised to the prediction of bursts. This needs further study.

Figure 10 presents the probability density distributions of skewness for tests conducted in the low-turbulence flume. Results suggest that the most probable values are positive rather than zero. This is consistent with the average values of skewness, further confirming the inappropriate performance of a Gaussian distribution.

Figure 11 illustrates the distributions of flatness for tests in the low-turbulence flume. The most frequently occurring values were found to be larger than 3, the typical value for a Gaussian distribution. This is in accordance with the average value of flatness.

Table 1. Statistical parameters of streak spacing, comparisons with literature.

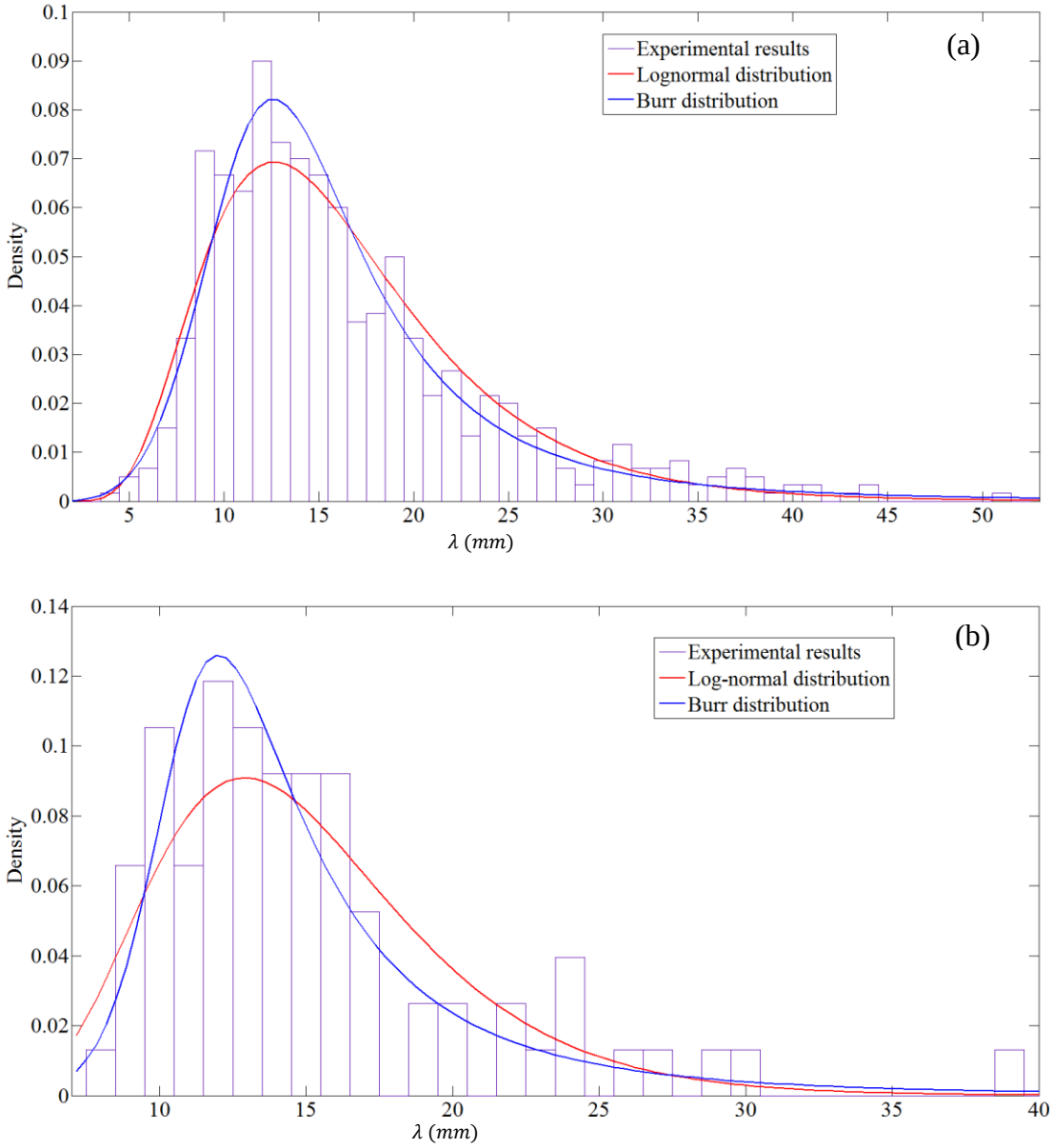

Figure 9. Probability density functions of streak spacing λ at y = 0.8mm ($y^+ = 6$), unidirectional turbulent current in the low-turbulence flume: (a) PIV measurements; (b) hydrogen bubble visualisations.

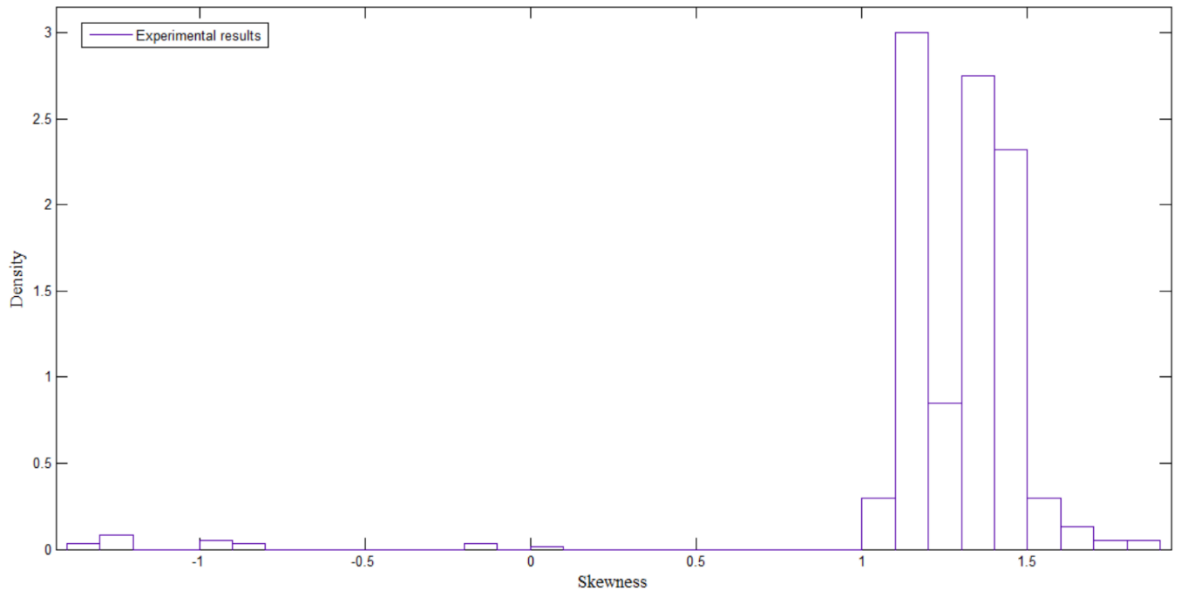

Figure 10. Probability density functions of skewness at $y = 0.8$mm ($y^+ = 6$), unidirectional turbulent current in the low-turbulence flume, PIV measurements.

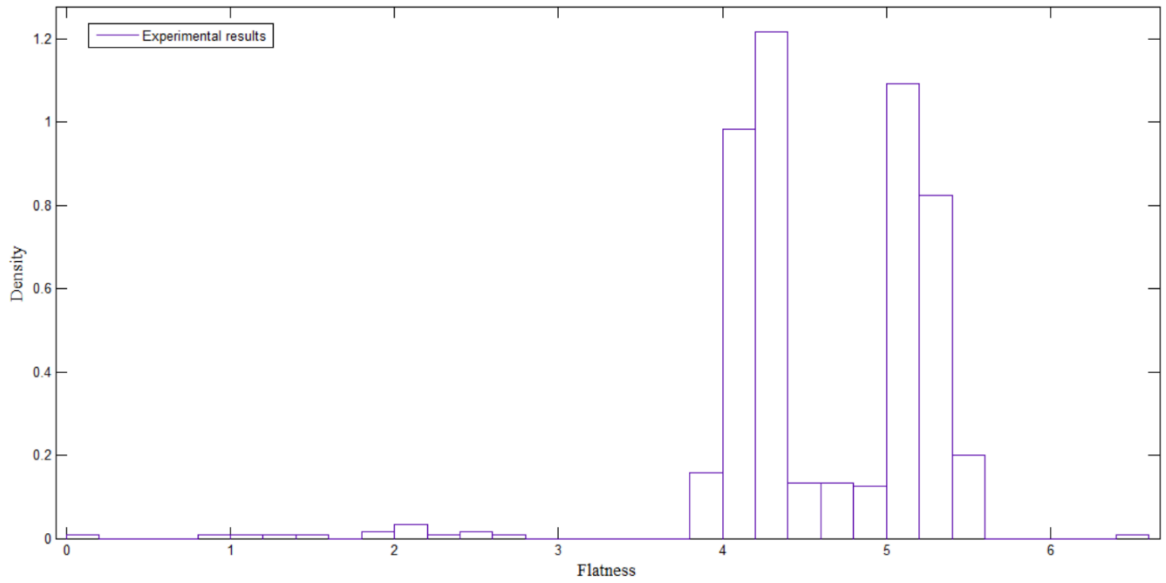

Figure 11. Probability density functions of flatness at $y = 0.8$mm ($y^+ = 6$), unidirectional turbulent current in the low-turbulence flume, PIV measurements.

4.2 Ejections and sweeps

Typical sequences of the instantaneous velocity field are presented in Figures 12 and 13 for the turbulent current flow tested in the two flumes. Contours of vorticity magnitude are plotted, together with velocity vectors after subtracting the speed of the moving reference frame U_c. Since there is no theoretical basis for the choice of U_c (Adrian et al., 2000), different values have been tested and $U_c = 0.8\,U_\infty$ is adopted here, as it is found to be the most appropriate to highlight hairpin vortices for tests in both flumes. Incidentally, Adrian et al. (2000) define a vortex as a region of concentrated vorticity around roughly circular streamlines when viewed in a frame moving with the vortex centre. Because of the 2D measurements obtained in the present study, the method of Herrera and Pallares (2013) to identify vortex cores was not used here.

Spanwise vortices are observed in both tests as highlighted using red ellipses. Shear layers are observed and highlighted by red lines, with spanwise vortices below the leading edge. Ejections are observed to occur continuously beneath the shear layer, agreeing with Adrian et al. (2000). These shear layers are inclined to the wall at 30°. This inclination angle should be differentiated from the inclination angle of the horseshoe vortex head. The original conceptual model (Theodorsen, 1952) suggests that the head of the horseshoe vortex is inclined to the bed at 45°. Smith (1984) also noted that a horseshoe vortex is inclined at 45°, while an array of

horseshoe vortices forms a shear layer inclined to the bed at 15° - 30°. A more recent study of Adrian et al. (2000) suggests that near-wall shear layers are inclined at 30° - 50°. The value of 30° as observed from the present study regardless of water depths further supports previous experiments. The presence of the shear layer with a spanwise vortex is consistent with existence of the horseshoe vortex, alternatively known as a hairpin vortex. Applying the Taylor hypothesis again, these vortices and shear layers move downstream approximately at the local mean velocity.

There are cases where two or more vortices merge into a single vortex, with a typical example shown in Figure 14. As can be seen from Figure 14 (a) to (c), the new vortex is longer in the streamwise direction and maintains its length scale in the vertical direction. The non-dimensional time (Δt^+) for the whole merging process was found to be 16. After the merging process, the new vortex moves downstream at the local mean velocity again.

Contour plots illustrated above are consistent with the model (Kline et al., 1967; Grass, 1971; Grass et al., 1991, 1993; Adrian et al., 2000) that ejections and sweeps are induced by the passage of hairpin vortices. Variations of fractional contributions from the two events are presented in Figure 15. Agreement with previous results (i.e. Moser et al., 1999; Wallace, 2016) is found. Although the present experiments have larger Reynolds numbers, Moser et al. (1999) suggest that theirs was sufficiently large to avoid Reynolds number effects.

Existing knowledge of unidirectional turbulent currents has confirmed the negative contributions from interaction events (Q1 and Q3 events) in generating Reynolds shear stress, and the dominance of ejections (Q2) over sweeps (Q4) away from the wall. The present results further support this. PIV measurements obtained from the present study show a reasonable agreement with previous results (Wallace et al., 1972; Lu and Willmarth, 1973; Brodkey et al., 1974; Kim et al., 1987; Schultz and Flack, 2007; Mejia-Alvarez and Christensen, 2010; Min, 2013). There is a good agreement between the shape of Q4 contributions, which does show an increase from y^+=10 to y^+=35. Results suggest values of 78% and 65% for the low-turbulence flume test, and 67% and 61% for the 16m flume test. Although there is no consensus on the fractional quadrant contributions to Reynolds shear stress, previous studies have confirmed the relative strength of Q2 events over Q4 events above the balance point. The ratios of Q2/Q4 are 1.2 and 1.1 for the two tests, both indicating that ejections contribute more to Reynolds shear stress than sweeps. The crossing point was found to be located at y^+=12 and in agreement with Kim et al. (1987). The only difference from the previous results is in the near-wall region (y^+ <10), which is caused by the lack of data very close to the bed because of the high reflection from the glass bed.

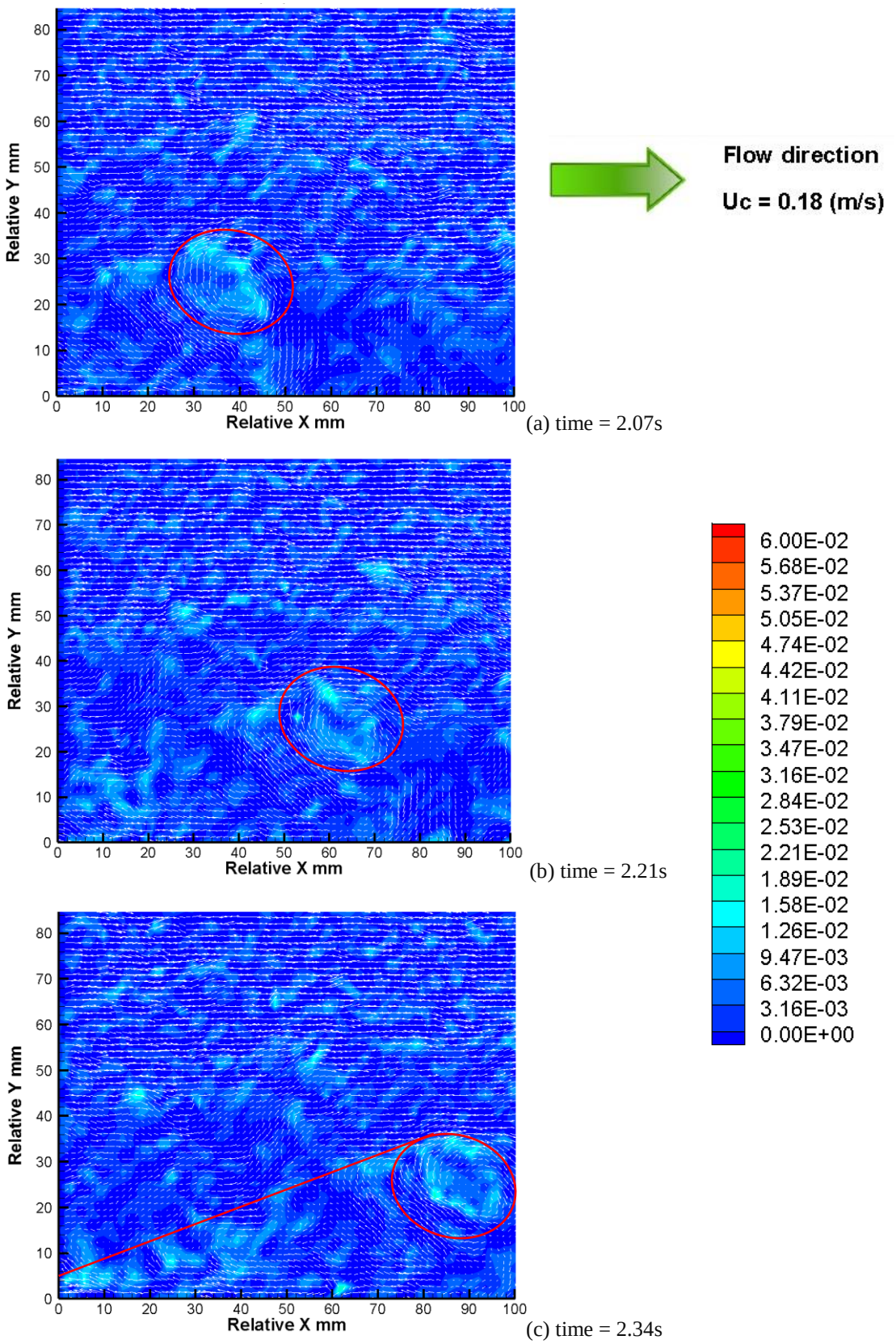

Figure 12. Time series of velocity vectors and vorticity ($10^3 \times s^{-1}$) contours, values of contours given in the legend, unidirectional turbulent current in the low-turbulence flume, PIV measurements at the flume centre, side view.

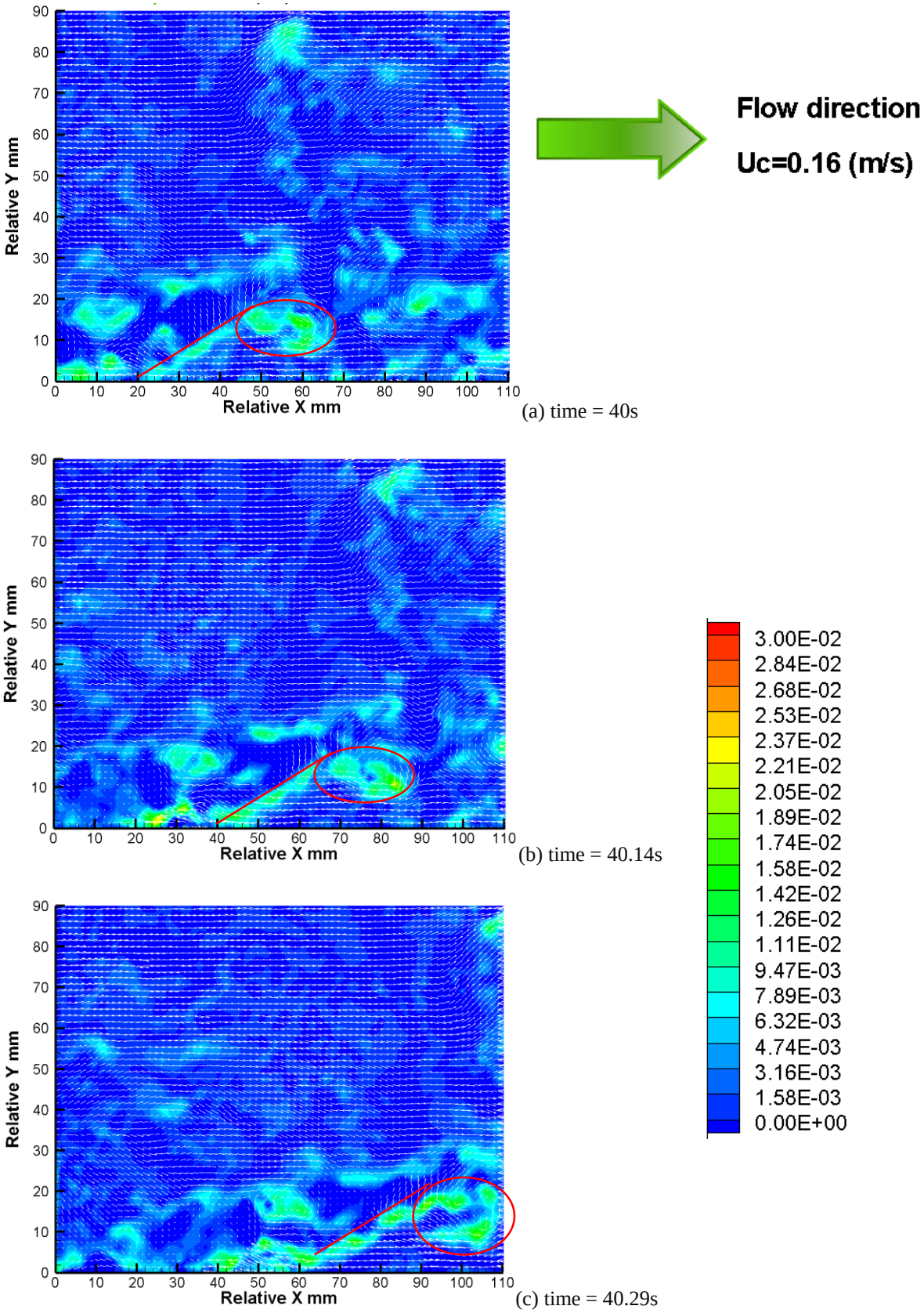

Figure 13. Time series of velocity vectors and vorticity ($10^3 \times s^{-1}$) contours, values of contours given in the legend, unidirectional turbulent current in the 16m flume, PIV measurements at the flume centre, side view.

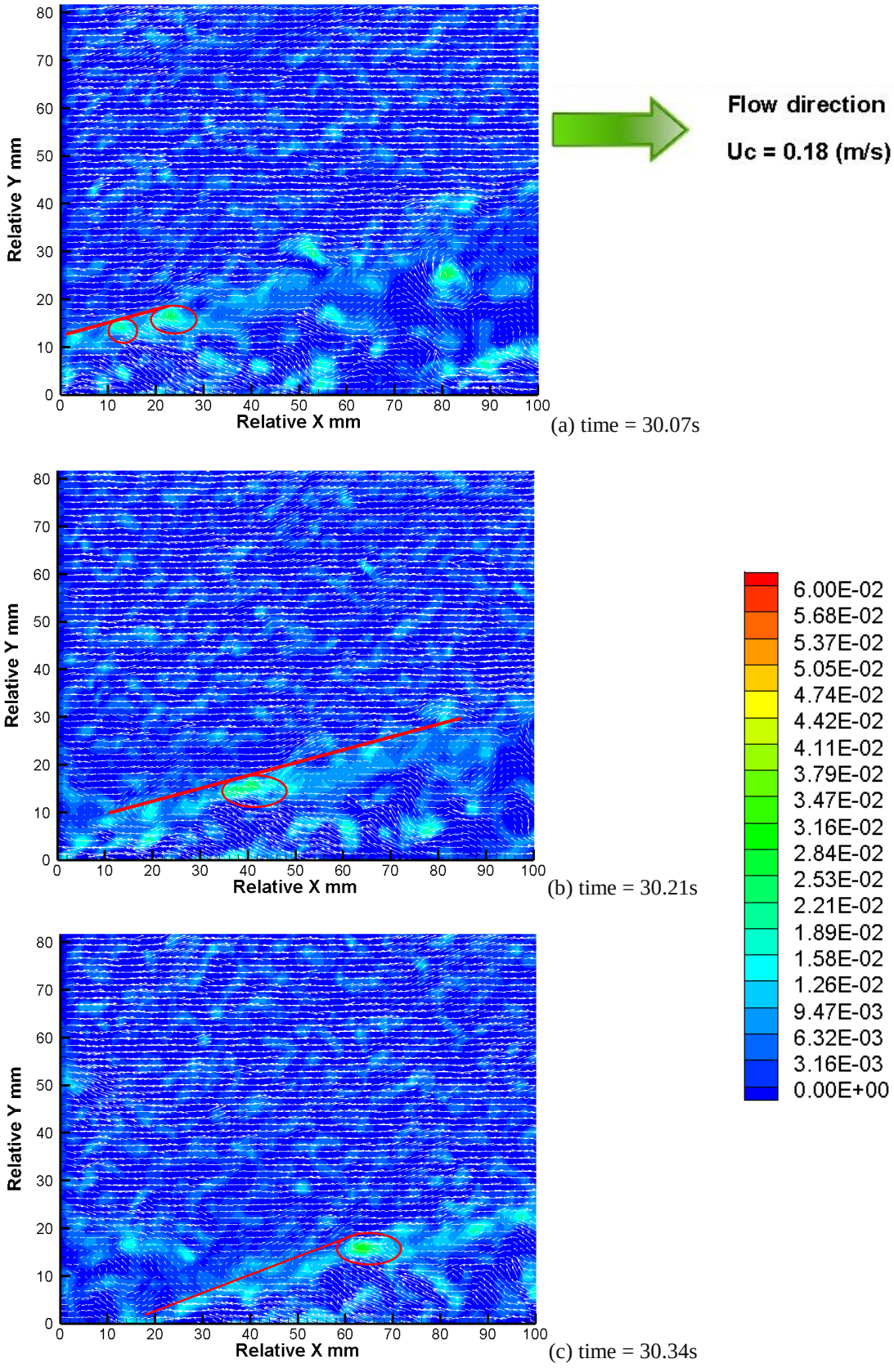

Figure 14. Time series of velocity vectors and vorticity ($10^3 \times s^{-1}$) contours, values of contours given in the legend, unidirectional turbulent current in the low-turbulence flume, PIV measurements at the flume centre, side view.

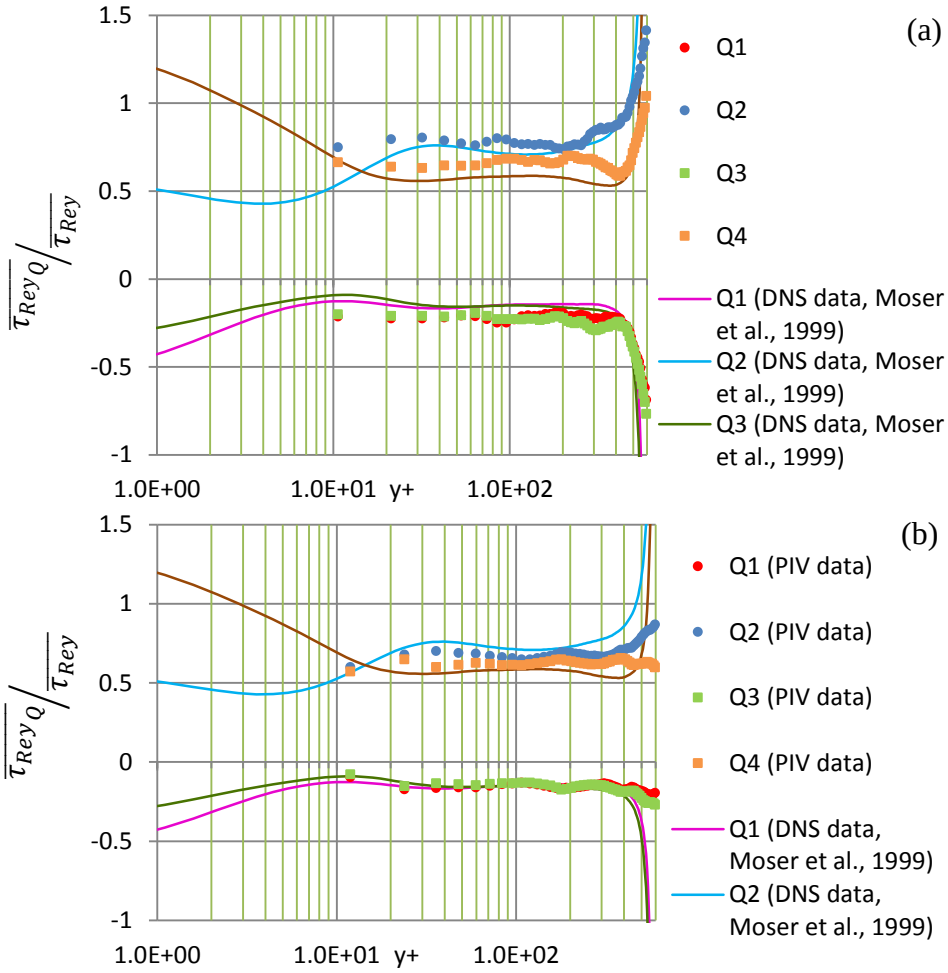

Figure 15. Quadrant contributions to the mean Reynolds shear stress: (a) low-turbulence flume; (b) 16m flume.

5. Conclusions

In the present study, experiments were performed in two laboratory flumes with different scales to examine the characteristics of coherent structures in turbulent boundary layers. A combined method of PIV and hydrogen bubble visualisation techniques was adopted to measure the flow field. The velocity fields in both the horizontal and vertical planes were used to identify and characterise the coherent patterns. The consistency of results between tests conducted in the two flumes demonstrates that the characteristics of turbulent coherent structures are essentially the same regardless of water depth, flume scale, and measurement techniques. The main conclusions obtained from the present project are summarised as follows:

1. Low-speed streaks are elongated in the streamwise direction and tend to meander in the spanwise direction. The streamwise length scale of low-speed and high-speed streaks can be up to maximum values of 5180 and 2330 viscous lengths respectively. In the spanwise direction, streaky patterns are tilted to the x-direction at a maximum tilting degree of 8°. The width of low-speed streaks (high-speed streaks) ranges between 7 and 110 (30 and 210) viscous lengths.
2. The streak spacing is linearly related to the integral spatial scale I.S.S, and the relationship $\lambda = 6*I.S.S$ is valid regardless of laboratory scale, water depth, and measurement techniques. This provides a new method to determine the spacing between low-speed streaks and can be generalised for future studies because of its simplicity and accuracy.
3. The probability density functions of streak spacing are better represented by a Burr distribution compared with the lognormal distribution found by previous authors for a unidirectional turbulent current.
4. The findings have engineering implications for sediment transport. Previous work on unidirectional turbulent currents (Nakagawa and Nezu, 1981) has shown that the probability density function of streak spacing is the same as that for bursting frequency. Thus, the new probability function for streak spacing can be used to derive a new probabilistic model for sediment resuspension.
5. Streak-merging processes are observed to occur repetitively for both low-speed streaks in the horizontal plane and spanwise vortices in the vertical plane. The former leads to a wider streak and the

latter results in vortices with larger diameters. The merging of turbulent streaks and spanwise vortices both takes time of $\Delta t^+ = 16$. This provides some evidence that there may be an association between vortex-pairing concepts and streak coalescence.

6. In the vertical plane, shear layers are inclined to the wall at 30°. Ejections occurring continuously beneath the shear layers. Quadrant analysis of Reynolds shear stress confirms the relative strength of ejection events over sweep events in the region of $y^+ > 12$.

Acknowledgements

The authors gratefully appreciate for the financial support from the UCL Dean's Prize and the China Scholarship Council (CSC). This work was supported by the National Natural Science Foundation of China (Grant No. 51909074), China Postdoctoral Science Foundation (Grant No. 2019M661713), and Key Laboratory of Coastal Disaster and Defence of Ministry of Education, Hohai University (Grant No. 201912).

References

Adrian, R.J., 1991. Particle-imaging techniques for experimental fluid mechanics. Annual review of fluid mechanics, 23(1), 261-304.

Adrian, R.J. and Liu, Z.C., 2002. Observation of vortex packets in direct numerical simulation of fully turbulent channel flow. Journal of visualization, 5(1), 9-19.

Adrian, R.J., Meinhart, C.D., Tomkins, C.D., 2000. Vortex organization in the outer region of the turbulent boundary layer. Journal of Fluid Mechanics, 422, 1-54.

Bakewell Jr, H.P. and Lumley, J.L., 1967. Viscous sublayer and adjacent wall region in turbulent pipe flow. The Physics of Fluids, 10(9), 1880-1889.

Blackwelder, R.F., 1983. Analogies between transitional and turbulent boundary layers. The Physics of fluids, 26(10), 2807-2815.

Blackwelder, R.F. and Eckelmann, H., 1979. Streamwise vortices associated with the bursting phenomenon. Journal of Fluid Mechanics, 94(3), 577-594.

Brodkey, R.S., Wallace, J.M. and Eckelmann, H., 1974. Some properties of truncated turbulence signals in bounded shear flows. Journal of Fluid Mechanics, 63(2), 209-224.

Burr, I.W., 1942. Cumulative frequency functions. The Annals of mathematical statistics, 13(2), 215-232.

Corino, E.R., and Brodkey, R.S., 1969. A visual investigation of the wall region in turbulent flow. Journal of Fluid Mechanics, 37, 1-30.

Chung, B., Cohrs, M., Ernst, W., Galdi, G.P. and Vaidya, A., 2016. Wake–cylinder interactions of a hinged cylinder at low and intermediate Reynolds numbers. Archive of Applied Mechanics, 86(4), 627-641.

Dennis, D.J., 2015. Coherent structures in wall-bounded turbulence. Anais da Academia Brasileira de Ciências, 87(2), 1161-1193.

Grass, A.J., 1971. Structural features of turbulent flow over smooth and rough boundaries. Journal of Fluid Mechanics, 50, 233-255.

Grass, A.J., Stuart, R.J., Mansour-Tehrani, M., 1991. Vortical Structures and Coherent Motion in Turbulent Flow over Smooth and Rough Boundaries. Physical Sciences and Engineering, 336, 35-65.

Grass, A.J., Stuart, R. J., Mansour-Tehrani, M., 1993. Common vortical structure of turbulent flows over smooth and rough boundaries. AIAA Journal, 31, 837-847.

Gyr, A. and Schmid, A., 1997. Turbulent flows over smooth erodible sand beds in flumes. Journal of hydraulic research, 35(4), 525-544.

Haidari, A.H. and Smith, C.R., 1994. The generation and regeneration of single hairpin vortices. Journal of Fluid Mechanics, 277, 135-162.

Heathershaw, A.D. and Thorne, P.D., 1985. Sea-bed noises reveal role of turbulent bursting phenomenon in sediment transport by tidal currents. Nature, 316(6026), 339.

Herrera, B. and Pallares, J., 2013. Identification of vortex cores of three-dimensional large-vortical structures. Archive of Applied Mechanics, 83(9), 1383-1391.

Insight 4G software Manual, Revision C, 2015.

Jeong, J., Hussain, F., Schoppa, W. and Kim, J., 1997. Coherent structures near the wall in a turbulent channel flow. Journal of Fluid Mechanics, 332, 185-214.

Jiménez, J., 2013. Near-wall turbulence. Physics of Fluids, 25(10), 101302.

Jiménez, J. and Kawahara, G., 2013. Dynamics of wall-bounded turbulence. Ten Chapters in Turbulence. 221-268.

Kasagi, N., Hirata, M. and Nishino, K., 1986. Streamwise pseudo-vortical structures and associated vorticity in the near-wall region of a wall-bounded turbulent shear flow. Experiments in fluids, 4(6), 309-318.

Keylock, C.J., Lane, S.N. and Richards, K.S., 2014. Quadrant/octant sequencing and the role of coherent structures in bed load sediment entrainment. Journal of Geophysical Research: Earth Surface, 119(2), 264-286.

Kasagi, N., Hirata, M. and Nishino, K., 1986. Streamwise pseudo-vortical structures and associated vorticity in the near-wall region of a wall-bounded turbulent shear flow. Experiments in fluids, 4(6), 309-318.
Kim, J., Moin, P. and Moser, R., 1987. Turbulence statistics in fully developed channel flow at low Reynolds number. Journal of fluid mechanics, 177, 133-166.
Kline, S.J., Reynolds, W.C., Schraub, F.A., and Runstadler, P.W., 1967. The structure of turbulent boundary layers. Journal of Fluid Mechanics, 30, 741-773.
Kim, H.T., Kline, S.J., and Reynolds, W.C., 1971. The production of turbulence near a smooth wall in a turbulent boundary layer. Journal of Fluid Mechanics, 50, 133-160.
Kim, J., Moin, P. and Moser, R., 1987. Turbulence statistics in fully developed channel flow at low Reynolds number. Journal of fluid mechanics, 177, 133-166.
Lagraa, B., Labraga, L. and Mazouz, A., 2004. Characterization of low-speed streaks in the near-wall region of a turbulent boundary layer. European Journal of Mechanics-B/Fluids, 23(4), 587-599.
Lee, S. H., Kim, J. H., and Sung, H. J., 2008. PIV measurements of turbulent boundary layer over a rod-roughened wall. International Journal of Heat and Fluid Flow, 29(6), 1679-1687.
Lelouvetel, J., Bigillon, F., Doppler, D., Vinkovic, I. and Champagne, J.Y., 2009. Experimental investigation of ejections and sweeps involved in particle suspension. Water resources research, 45(2).
Lu, S.S. and Willmarth, W.W., 1973. Measurements of the structure of the Reynolds stress in a turbulent boundary layer. Journal of Fluid Mechanics, 60(3), 481-511.
Mansour-Tehrani, M., 1992. Spatial distribution and scaling of bursting events in boundary layer turbulence over smooth and rough surfaces. Ph.D. Thesis, University of London.
Mejia-Alvarez, R. and Christensen, K.T., 2010. Low-order representations of irregular surface roughness and their impact on a turbulent boundary layer. Physics of fluids, 22(1), 015106.
Min, D., 2013. Combined irregular roughness and favorable-pressure-gradient effects in a turbulent boundary layer. Ph.D. Thesis, University of Illinois at Urbana-Champaign.
Moser, R.D., Kim, J. and Mansour, N.N., 1999. Direct numerical simulation of turbulent channel flow up to $Re_\tau = 590$. Physics of fluids, 11(4), 943-945.
Nakagawa, H. and Nezu, I., 1981. Structure of space-time correlations of bursting phenomena in an open-channel flow. Journal of Fluid Mechanics, 104, 1-43.
Nelson, J.M., Shreve, R.L., McLean, S.R. and Drake, T.G., 1995. Role of near-bed turbulence structure in bed load transport and bed form mechanics. Water resources research, 31(8), 2071-2086.
Oldaker, D.K. and Tiederman, W.G., 1977. Spatial structure of the viscous sublayer in drag-reducing channel flows. The Physics of Fluids, 20(10), S133-S144.
Robinson, S.K., 1991. Coherent motions in the turbulent boundary layer. Annual of Review of Fluid Mechanics, 23, 601-639.
Schultz, M.P. and Flack, K.A., 2007. The rough-wall turbulent boundary layer from the hydraulically smooth to the fully rough regime. Journal of Fluid Mechanics, 580, 381-405.
Sleath, J.F.A., 1984. Sea bed mechanics. John Wiley & Sons Press, New York, U.S.
Smith, C.R. and Schwartz, S.P., 1983. Observation of streamwise rotation in the near-wall region of a turbulent boundary layer. The Physics of Fluids, 26(3), 641-652.
Smith, C.R., 1984. A synthesized model of the near-wall behavior in turbulent boundary layers. In Proc. 8th Symp. on Turbulence, 299-325, University of Missouri-Rolla.
Smith, C. R., and Metzler, S. P., 1983. The characteristics of low-speed streaks in the near-wall region of a turbulent boundary layer. Journal of Fluid Mechanics, 129, 27-54.
Smith, C. and Walker, J., 1998. Sustaining mechanisms of turbulent boundary layers-The role of vortex development and interactions. In 29th AIAA, Fluid Dynamics Conference, 2959.
Stretch, D.D., 1990. Automated pattern eduction from turbulent flow diagnostics. Center for Turbulence Research Annual Research Briefs, 145-157.
Stuart, R.J., 1984. Three-dimensional characteristics of coherent flow structures in a turbulent boundary layer over a rough surface. Ph.D. Thesis, University of London.
Sutherland, A.J., 1967. Proposed mechanism for sediment entrainment by turbulent flows. Journal of Geophysical Research, 72(24), 6183-6194.
Tadikamalla, P.R., 1980. A look at the Burr and related distributions. International Statistical Review, 48, 337-344.
Taylor, G.I., 1938. The spectrum of turbulence. Proceedings of the Royal Society of London. Series A, Mathematical and Physical Sciences, 476-490.
Theodorsen, T., 1952. Mechanism of turbulence. Proceedings of the Midwestern Conference on Fluid Mechanics, Ohio State University, Columbus.
Wallace, J.M., 2016. Quadrant analysis in turbulence research: history and evolution. Annual Review of Fluid Mechanics, 48, 131-158.

Wallace, J.M., Eckelmann, H. and Brodkey, R.S., 1972. The wall region in turbulent shear flow. Journal of Fluid Mechanics, 54(1), 39-48.

Zhang, X. and Simons, R., 2019. Experimental investigation on the structure of turbulence in the bottom wave-current boundary layers. Coastal Engineering, 152, p.103511.

Table 1. Statistical parameters of streak spacing, comparisons with literature.

Investigators	The most probable value $\lambda_{most}\ (mm)$	Non-dimensional most probable value ${\lambda_{most}}^{+}$	Standard deviation $\sigma_\lambda\ (mm)$	Coefficient of variation ψ_λ	Skewness S_λ	Flatness F_λ
Present study in the low-turbulence flume, results from PIV measurements	12	90	7	0.45	1.36	4.98
Present study in the low-turbulence flume, results from hydrogen bubble measurements	12	90	6	0.37	1.71	6.57
Present study in the 16m flume	12	89	8	0.47	1.50	5.50
Oldaker and Tiederman (1977)	Not given	Not given	Not given	0.36	Not given	Not given
Smith and Metzler (1983)	Not given	78	Not given	Ranges from 0.4 to 0.5	Ranges from 0.6 to 1.0	Ranges from 3 to 4
Mansour-Tehrani (1992)	Ranges from 8 to 30.	Ranges from 80 to 90	Ranges from 4 to 13.	Ranges from 0.35 to 0.39	Ranges from 0.67 to 0.91	Ranges from 3.9 to 4.2